Imperfect chimera and synchronization in a hybrid adaptive conductance based exponential integrate and fire neuron model

Sathiyadevi Kanagaraj[1], Irene Moroz[2], Premraj Durairaj[1], Anitha Karthikeyan[3,4] and Karthikeyan Rajagopal[1*]

[1]Centre for Nonlinear Systems, Chennai Institute of Technology, Chennai, 600 069, Tamilnadu, India.
[2]Mathematical Institute, Oxford University, Oxford, OX2 6GG, United Kingdom.
[3]Department of Electronics and Communication Engineering, Vemu Institute of Technology, Chitoor, 517112 Andhra Pradesh, India.
[4]Department of Electronics and Communications Engineering and University Centre for Research & Development, Chandigarh University, Mohali, 140 413, Punjab, India.

*Corresponding author(s). E-mail(s): rkarthiekeyan@gmail.com;
Contributing authors: sathiyadevik@gmail.com;
Irene.Moroz@maths.ox.ac.uk; premraj2891@gmail.com;
Mrs.anithakarthikeyan@gmail.com;

Abstract

In this study, the hybrid conductance-based adaptive exponential integrate and fire (CadEx) neuron model is proposed to determine the effect of magnetic flux on conductance-based neurons. To begin with, bifurcation analysis is carried out in relation to the input current, resetting parameter, and adaptation time constant in order to comprehend dynamical transitions. We exemplify that the existence of period-1, period-2, and period-4 cycles depends on the magnitude of input current via period doubling and period halving bifurcations. Furthermore, the presence of chaotic behavior is discovered by varying

the adaptation time constant via the period doubling route. Following that, we examine the network behavior of CadEx neurons and discover the presence of a variety of dynamical behaviors such as desynchronization, traveling chimera, traveling wave, imperfect chimera, and synchronization. The appearance of synchronization is especially noticeable when the magnitude of the magnetic flux coefficient or the strength of coupling strength is increased. As a result, achieving synchronization in CadEx is essential for neuron activity, which can aid in the realization of such behavior during many cognitive processes.

1 Introduction

Computational neuroscience has recently received tremendous attention among researchers since it helps to unravel numerous biological processes [1, 2]. For instance, to better understand the neural activity during the cognitive processes, various biological neuron models have been developed including FitzHugh-Nagumo (FHN), Hindmarsh-Rose (HR), Hodgkin-Huxley (HH), Izhikevich (IZH) and so on [3–7]. For instance, the dynamical patterns in a network of FitzHugh-Nagumo oscillators have been examined using various network connectivities such as regular, random, nonlocal, small-world, ring networks with fractal network connectivities [8–10]. Fitzhugh-Nagumo oscillators with an empirical structural connection can exhibit spontaneous synchronization similar to that found during epileptic seizures in humans [11]. The occurrence of lag synchronization has been demonstrated using a network of time-delayed FHN with feedback control [12]. The reflection connection among the nodes in the FHN network can result in chimera-like hybrid dynamical behaviors with coexisting coherent and incoherent behaviors [13]. The effect of bifurcation delay generated synchronization and desynchronization in slow-fast systems has been studied by varying a slowly varying parameter [14]. The intermittent and anti-phase synchronization was recently discovered when the FHN neurons were coupled by nonlinear memductance [15].

Recently, the filtering capabilities of HH neurons have been investigated and the required band pass filtered signal can be witnessed by adjusting the upper and lower cut-off frequencies [16]. The diagnosis of COVID-19 disease in patients' X-ray images has been revealed by developing a hybrid model of 2D curvelet transform that employs the chaotic salp swarm algorithm and deep learning technique [17]. Analogously, a hybrid classification model based on swarm optimization has been implemented to diagnose the plant disease [18]. More recently, periodic/hyperchaotic spiking and bursting patterns have been obtained by coupling two Morris-Lecar neurons via a memristor synapse [19]. A piecewise-linear Hopfield neural network with memristor synapse coupling can exhibit multistability of coexisting chaos, periodic limit cycles, and stable point attractors [20]. Moreover, it is revealed that memristive neurons are used

in the development of neuromorphic sensing, computing systems, humanoid robots with high energy efficiency, pattern recognition, and so on [21–23].

To illustrate the dynamics of the brain network, the functional brain network was built employing HR neurons as nodes in the brain regions [24]. The birth and death of spiral wave patterns were delineated in extended HR neurons when applying external magnetic excitations and discontinuous exponential flux coupling [25, 26]. Importantly, diverse bursting and spiking patterns were discovered in modified fractional-order HR neurons [27]. The Izhikevich neuron model can result in a variety of spiking patterns, such as regular, resonance, chattering, fast, chaotic spiking, and chaotic bursts, when subjected to external excitations and noise [28]. Using the fractional-order Izhikevich neuron model, synchronization and FPGA realizations were also delineated [29]. Similarly, the neural activities of cognitive systems were manifested by utilizing distinct other neuronal models by incorporating various factors such as external excitations, time-delay, memristor function, and so on, as well as numerous complex network connectivities [31–33].

Additionally, a variety of current and conductance-based neuron models have been developed due to their widespread applications in neural networks. By taking into account leaky Integrate-and-fire (LIF) neurons, the comparison dynamics of the current (voltage-independent) and conductance (voltage dependent)-based neurons have been examined [30]. It has been reported that the generalized LIF with variable resister (leaking) and bias current may precisely mimic the behavior of real neurons' membrane voltage [34]. The emergence of the spike train has been noticed when implementing the spike-frequency adaptation in such generalized LIF systems [35, 36]. The adaptive exponential IF neuron model was designed further to accurately mimic neural activity and get around the drawbacks of strict voltage threshold, subthreshold adaptation, and conductance-based stimulation, which brings the dynamics closer to the cortical neurons [37]. Increased adaptation currents in the adaptive exponential integrate-and-fire neurons model promote synchronization of the network of coupled excitatory neurons at low-frequency oscillations, while inhibitory neurons exhibit coherent behaviors at higher frequencies [38]. Neuron spike time adaptation was described using the fractional Leaky Integrate-and-Fire Model [39]. The existence of chimera state with spike and burst activity was identified depending on the nearest neighbors and coupling strength of the nonlocally coupled adaptive exponential integrate-and-fire (AEIF) neuron model [40]. The time-delay induced cluster synchronization and firing rate oscillation were reported in randomly interacted Adaptive Exponential Integrate-and-Fire (Ad-EIF) neurons [41].

Besides, the investigation reveals that conductance-based neuron models are effective at simulating biological behaviors, hardware implementation, and a digital programmable platform can be done at a low cost [42]. As a result, numerous studies have been carried out using conductance-based neuron models. In particular, the Wilson conductance-based neocortical neuron model has been employed to figure out the underlying mechanisms of the firing patterns,

and it has been found that, depending on the stimuli, spiking, bursting, chaotic firing, and subthreshold oscillations exist [43]. The presence of various collective behaviors, such as synchronization, chimera, and cluster states, has been identified using the flux-coupled conductance-based neuron by adding propagation noise to the system [44]. The emergence of various firing patterns has been detailed using isolated CadEx neurons without magnetic flux [45]. *Considering the aforementioned observations, it is clear that studies on the coupled version of CadEx neurons is limited. Importantly, the dynamical properties of CadEx neurons and their network behaviour have received little attention in the literature. To investigate the dynamical properties, we therefore, take into account CadEx neurons. In particular, we focus on the dynamical behavior of the system in the presence of magnetic flux. Primarily, the dynamical transitions with respect to input current, resetting parameter, and adaptation time constant and its bifurcation routes are examined using bifurcation analysis. Following that, we also discuss the network behaviors and transitions of the proposed hybrid CadEx neurons. We demonstrate that the transition to synchronization occurs via an imperfect transient chimera while increasing the coupling strength or magnetic coupling coefficients.*

The following is the structure of the manuscript: Sec. 2 introduces a hybrid conductance-based neuron model. In Sec. 3, the dynamical characteristics and transitions are investigated using bifurcation analysis with respect to the input current, adaptation time constant, and resetting threshold. Following that, the dynamical behavior of the CAdEx network is explored in Sec. 4. Finally, the overall results are summarized in Sec. 5.

2 Conductance neuron model

The adaptive exponential integrates and fire neuron model (AdEx) is familiar because of its low-cost implementation probability. But as this model depends on current-based adaptation, it shows some non-biophysical behaviors which are unrealistic to a neuron model. Hence in [45] the authors proposed a conductance-based adaptive exponential integrate and fire neuron model which they named as CadEx. Though this model can overcome the drawbacks of the AdEx model, it still can't consider the magnetic field effects. Applying external stimuli beyond the threshold can sometimes trigger static and dynamic charges. These dynamic moving charges can create magnetic fields and can have a significant effect on the neuron model. Hence, we modify the CadEx model to include the variation of magnetic field and electromagnetic induction by describing an additional state variable to the original CadEx model. The new modified CadEx model can be defined as,

$$C\dot{v} = G_L(v_L - v) + G_L M_{st} exp(\frac{v - v_\tau}{M_{st}}) + g_A(E_A - v) + I_s - k_0 M(\phi)v,$$

$$\tau_A \dot{g}_A = \frac{\bar{G_A}}{(1 + exp(\frac{v_A - v}{\delta_A}))} - g_A,$$
$$\dot{\phi} = k_1 v - k_2 \phi, \tag{1}$$

where v, g_A, and ϕ are the state variables of the hybrid CadEx neuron that represent membrane voltage, conductance-based adaptation, and magnetic flux, respectively. Typically, the memristors can exhibit the memory effect, which is used to recall the magnetic flux across the membrane of neurons or cells. Here, the magnetic flux induction is replicated using the memductance function of a memristor described by $M(\phi) = \alpha + 3\beta\phi^2$ where α and β are the fixed parameters [46–48]. k_0 is the flux coupling co-efficient. The terms $k_1 v$ and $k_2\phi$ denote the membrane potential induced changes on magnetic flux and leakage of magnetic flux, respectively. k_1 and k_2 are constant parameters. The resetting mechanism after the spike is defined by the rule

$$v \geq v_{_{Th}}, \begin{cases} v \rightarrow v_R, \\ g_A \rightarrow g_A + \delta_{g_A}. \end{cases} \tag{2}$$

We specifically set the parameter of the system(1) to chaotic like spiking [45] as given in Table (1). The other fixed parameters are set as $\alpha = 0.01$; $\beta = 0.01$; $k_0 = 0.1$; $k_1 = 0.1$; $k_2 = 0.5$. Unless otherwise specified, the parameters values of the system (1) are defined as follows throughout the text.

Table 1 Physical meaning of the parameters and its magnitudes

Parameters	Magnitudes
Membrane capacitance, C	200 pF
Leak conductance, G_L	10.0 nS
Reversal potential, v_L	-58 mV
Spike threshold, v_τ	-50 mV
Slope of the spike initiation, M_{st}	2.0
Reversal potential of the adaptation conductance, E_A	-70 mV
Input current, I_s	90 pA
Time constant of adaptation, τ_A	25.0 ms
Maximal subthreshold adaptation conductance, $\bar{G_A}$	10.0 nS
Subthreshold adaptation activation voltage, v_A	-40 mV
Slope of subthreshold adaptation, δ_A	5.0 nS
Reset potential, v_R	-47 mV
Reset voltage, $v_{_{Th}}$	-40 mV
Incremented quantal conductance after each spike, δ_{g_A}	1.0 nS

In this study, the Runge-kutta fourth order algorithm with a step size of $h = 0.01$ is used for numerical simulations.

2.1 The nullclines of the CadEx Model

Because of the exponential terms in Eq. (1), it is not possible to determine the exact analytical expression for the fixed points. Instead we follow Gorski (2021) and plot the v and g_A nullclines as functions $U_1 = g_A$ and $U_2 = g_A$ respectively, as v varies after substituting for the equilibrium value of $\phi = \frac{k_1 v}{k_2}$ into evolution equation for $v(t)$ [45].

$$\begin{aligned} U_{1a} &= \frac{(G_L(v_L - v) + G_L M_{st} exp(\frac{v - v_\tau}{M_{st}}) + I_s)}{(v - E_A)}, \\ U_{1b} &= \frac{-k_0 M(\phi) v}{(v - E_A)}, \\ U_1 &= \frac{(G_L(v_L - v) + G_L M_{st} exp(\frac{v - v_\tau}{M_{st}}) + I_s - k_0 M(\phi) v)}{(v - E_A)}, \\ U_2 &= \frac{\bar{G_A}}{(1 + exp(\frac{v_A - v}{\delta_A}))}. \end{aligned} \tag{3}$$

The equilibrium states of Eq. (1) are then obtained by noting the points of intersection of U_1 with U_2. Figure 1 shows plots of the U_1 (red curve) and U_2 (black) nullclines as varies, v for $I_s = 90$. Unlike the Gorski et al (2021) case, the presence of the magnetic induction term ϕ means the two nullclines do not intersect for our choice of parameter values. This figure is analogous to Fig. 2(a) in Gorski et al [45]. Gorski et al (2021) also plot the function I_s as a function of v [45]. If we write:

$$\begin{aligned} I_{s1} = -G_L\big((v_L - v) + M_{st} exp(\frac{v - v_\tau}{M_{st}})\big) \\ + \frac{G_A}{(1 + exp(\frac{v_A - v}{\delta_A}))}(v - E_A) \\ I_{s2} = k_0 M(\phi) v \end{aligned} \tag{4}$$

Then we can take I_{s1} to be $SV1$, the ϕ independent part of the total current, I_s, while the linear sum of $I_{s1} + I_{s2}$ is SV or I_s with ϕ included. Figure 2 shows those plots for our set of parameter values. The plots of $SV1$ (in black) are for the ϕ-independent systems, while SV (in red) are for the ϕ-dependent systems. In Figure 2 the curves of $SV1$ and $SV2$ intersect the lines of constant I_{ext} twice (indicating two possible fixed points). Figure 2(b) shows a blow-up of these plots near the maxima of the two curves. These maxima occur for $I_s \approx 86.814$ in the absence of ϕ ($SV1$: black curve), and at $I_s \approx 72.7045$ for SV (red curve). When we compare with the parameter choice for $I_s = 90$, this means that no fixed points are possible, since $I_s = 90$ lies above the maxima of both curves. This corroborates the results, shown in Fig. 1. If we anticipate the results from the bifurcation plots in the next section, we see that steady-state solutions are found in the lowest branch of the bifurcation plot. And so,

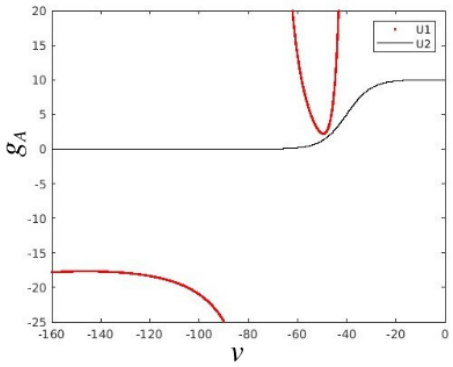

Fig. 1 The nullclines for the Cadex equations as v varies for the current set of parameter values, with $I_s = 90$. The red curve corresponds to the U_1 nullcline, and the black curve corresponds to the U_2 nullcline.

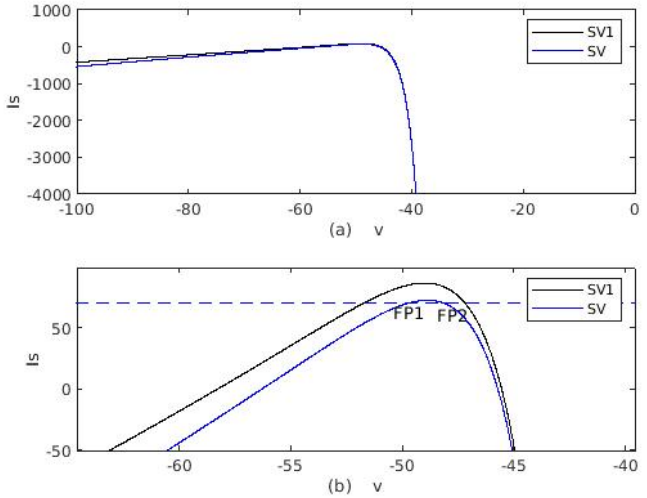

Fig. 2 The curves of the current I_s as functions of v. $SV1$ (in black) is for the ϕ-independent system, while SV (in blue) is when ϕ- is included. The lower plot is a blow-up of the region near the maxima of the two curves. For $SV1$ this occurs for $I_s \approx 86.814$, while for SV, this occurs for$I_s \approx 72.7045$. Also shown are the two fixed points $FP1$ and $FP2$ when $I_s = 70$.

for example, we indicate the location of the two fixed points in Fig. 3(b) for $I_s = 70$: FP1 occurs at $v \approx -49.79$, while FP2 occurs at $v \approx -48.09$.

3 Dynamical behaviors and its transition of a CadEx neuron

In order to comprehend the dynamical behaviors and its transition of system(1), we choose three different parameters including current (I_s), the

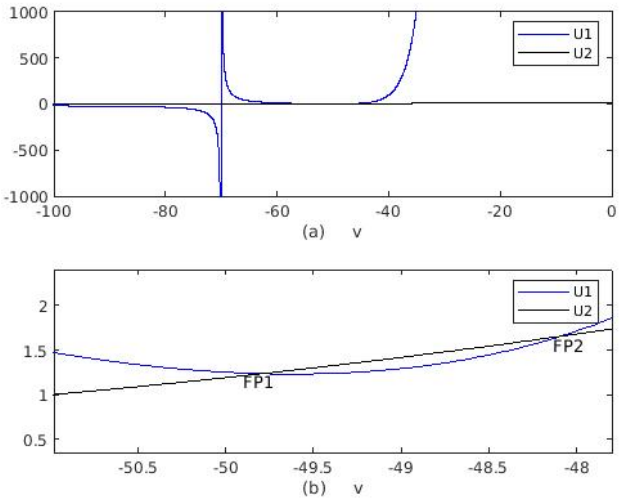

Fig. 3 As in Figure 1, but showing the nullclines for $I_s = 70$, v varies. There are now two fixed points, shown as $FP1$ and $FP2$ in Figure 3b.

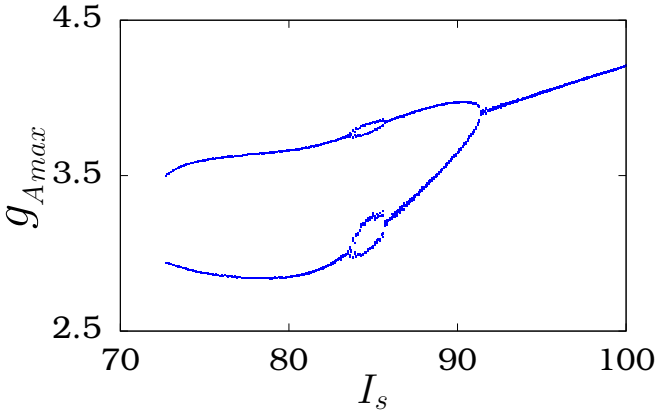

Fig. 4 The bifurcation transition plot of successive maxima of $g_{A_{max}}$ is obtained by fixing the resetting threshold $v_R = -47.0$ and adaptive time constant $\tau_a = 25.0$, as I_s is decreases between $70 \leq Is \leq 100$. The values for the other parameters are set as given in Table (1). The dynamical transitions via period doubling to period halving as a function of I_s.

resetting parameter (v_R) and adaptation time constant (τ_a). Figure 4 shows the bifurcation transition plot as I_s is decreased from $I_s = 100$ to $I_s = 70$ when all the remaining parameters of Eq. (1) are kept constant. Bifurcation transition is obtained by finding the successive $g_{A_{max}}$ maxima of each cycle with respect to I_s. We can note that the branch of periodic solutions extends from $I_s = 100$, undergoing a period-doubling bifurcation at $I_s = 91.59$. When decreasing the value of I_s further period-four cycle occurs at $I_s = 85.8$, which

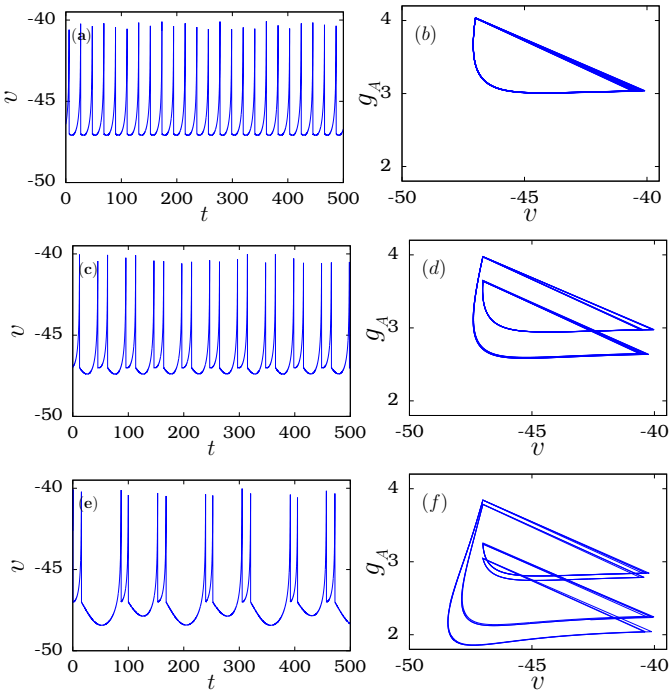

Fig. 5 Time evolutions and phase portrait trajectories for (a) period-1 orbit for $I_s = 95$, (b) period-2 orbit for $I_s = 90$, and (c) period-4 orbit for $I_s = 85$, where the resetting threshold is fixed at $v_R = -47.0$ and the adaptive time constant is set at $\tau_a = 25.0$. The values for the other parameters are set as given in Table (1). The occurrence of period-1, period-2, and period-4 orbits by varying the magnitude of the input current.

disappears at $I_s = 83.63$, leaving a period-two cycle, which itself disappears at $I_s = 72.71$. Therefore, the results clearly illustrate that the occurrence of period-1, period-2, and period-4 orbits dependent on the magnitude of I_s.

Figure 5 shows a section of the time series for the state variable v and the corresponding phase portraits in the (v, g_A)-plane. From Figs. 5 (a)-(b), it is clear that the emergence of period-1 cycle for $I_s = 95$. When decreasing the current to $I_s = 90$, we observed that the existence of period-2 cycle as shown in Figs. 5 (c)-(d). Further, decreasing $I_s = 85$ give rise to the period-4 cycle which is shown in Figs. 5 (e)-(f). From the phase portrait images displayed in Figs. 5(b), 5(d), and 5(f), respectively, it is easier to grasp the presence of the period-1, period-2, and period-4 cycles.

If we fix $I_s = 80$ and reduce the resetting parameter from $v_R = -40$ to $v_R = -70$, we get the bifurcation transition plot shown in Fig. 6(a). The inset denote the portion of bifurcation transition showing the period doubling transition to chaos as increasing v_R. When the range of v_R is increased further, the transition from chaotic to periodic state occurs via period halving bifurcation.

In addition, the bifurcation diagram is plotted in Fig. 6(b) to show the dyamical transition for $I_s = 90$. Importantly, we can observe that the decreasing of chaotic regions when increasing current (I_s). A periodic cycle loses its stability as v_R decreases to a period-two cycle at $v_R = -46.76$, which persists until it is lost in a period-halving bifurcation at $v_R = -47.55$. When the resetting parameter is $v_R = -47$, we can observe a period-two cycle.

The two parameter diagram is plotted in (I_s, v_R) space in Fig. 6(c) to help

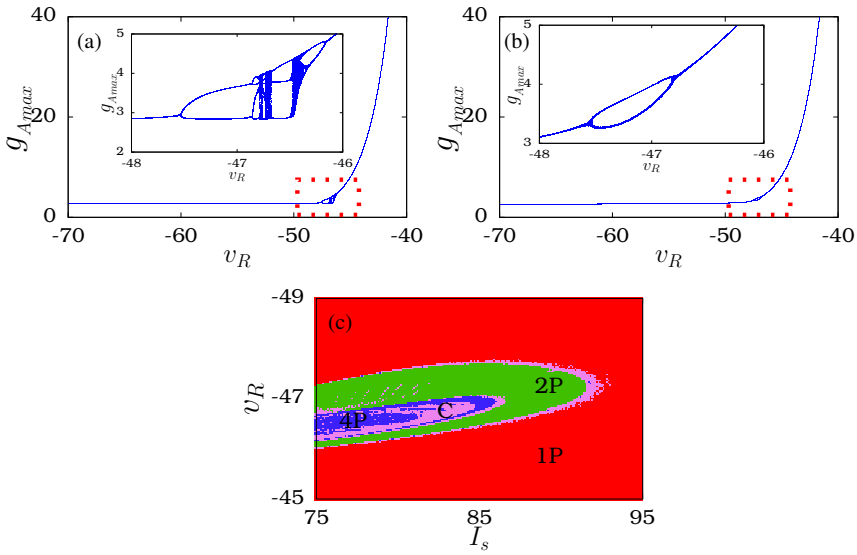

Fig. 6 The bifurcation transition plot of successive maxima of $g_{A_{max}}$, as v_R decreases between $v_R = -70$ and $v_R = -40$ for $\tau_a = 25.0$, (a) $I_s = 80$ and (b) $I_s = 90$. The inset in (a) and (b) denote the zoomed in view of the portion of bifurcation transition in a red dashed line. (c) Two parameter diagram in (I_s, v_R) space by fixing $\tau_a = 25$. P, 2P, and 4P denote the one-periodic, two-periodic and four-periodic orbits, respectively. C denote the chaotic region. The values for the other parameters are set as given in Table (1).

understand the dynamical transitions in parameter space. When the range of stimuli current is between $75 \lessapprox I_s \lessapprox 86$, increasing the resetting threshold exhibits the transition from one-periodic (P) state to two periodic (2P), four periodic (4P) to chaos (C), then increasing vR exhibits the inverse transition from Chaos to 4P, 2P and 1P. The 4P state is suppressed while increasing the I_s in the range $86.1 \lessapprox I_s \lessapprox 91.7$. It is observed periodic state for entire range of v_R at large values of I_s. While nearly all of the parameter values of Eq. (1) are similar to those of Gorski et al (2021), apart from I_s, the other parameter that differs widely is τ_a, the time constant of adaptation. Gorski et al (2021) take $\tau_a = 500$, while we take $\tau_a = 25$. It is therefore of interest to see what the consequences are for the dynamics of the system by varying τ_a between these two extremes. Figure 7 shows a portion of the bifurcation transition diagram between $20 \leq \tau_a \leq 80$. We actually increased τ_a to $\tau_a = 500$. Apart from

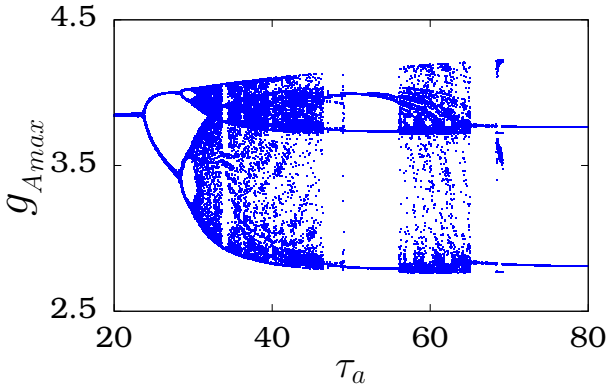

Fig. 7 The bifurcation transition plot of successive maxima of $g_{A_{max}}$, as τ_a decreases between $\tau_a = 20$ and $\tau_a = 80$ by fixing $v_R = -47.0$ and I_s=90. The scattered points represent the presence of chaotic attractors. The values for the other parameters are set as given in Table (1). The transition to chaotic dynamics via period doubling bifurcation while increasing the time adaptation constant (τ_a).

a lengthening of the period of oscillations as τ_a increases, we found no more transitions. For $\tau_a = 23.85$ the period-two cycle loses stability to a period-four cycle ($\tau_a = 28.33$), which in turn loses stability to a period-eight cycle at $\tau_a = 29.95$. As τa is increased further, we could see the chaotic behaviour that displays the scattered points in the bifurcation diagram.

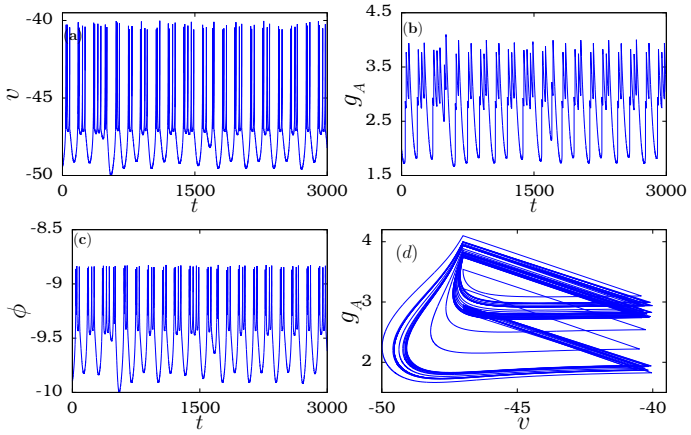

Fig. 8 The temporal evolution of chaotic state for the state variables (a) v, (b) g_A, and (c) ϕ, by fixing $\tau_a = 40$, $I_s = 90$, and $v_R = -47.0$. (d) The phase portrait trajectory of chaotic state in (v, g_A) space. The values for the other parameters are set as given in Table (1).

In Fig. 8, we presented the temporal evolution of the system in terms of the state variables to demonstrate the occurrence of chaotic spiking while fixing $\tau_a = 40$. The formation of chaotic spiking is seen from Figs. 8(a) - 8(c) in terms

of the state variables v, g_A, and ϕ, respectively. For a better understanding of the trajectory of chaotic spiking behaviors, we also plotted the phase portrait diagram in (v, g_A) space, which also manifests the chaotic behavior of the system for the specified set of parameters. With this understanding of CadEx neuron dynamical behaviors, we extend the analysis to the network case in the following.

4 Collective dynamics of a network of cadex neurons

In a realistic situation, the neurons must communicate with one another in order to perform specific cognitive tasks. Thus, it is intriguing to investigate the collective behavior of a large set of neurons when they are coupled together. As consequence, we consider a ring network of nonlocally coupled CadEx neurons, and the corresponding dynamical expressions can be written as

$$\begin{aligned} C\dot{v}_j &= G_L(v_L - v_j) + G_L M_{st} exp(\frac{v_j - v_\tau}{M_{st}}) + g_{A_j}(E_A - v_j) \\ &\quad + I_s - k_0 W(\phi_j) v_j + \frac{D}{2P} \sum_{k=l-P}^{l+P} (v_k - v_j), \\ \tau_A \dot{g}_{A_j} &= \frac{\bar{G_A}}{(1 + exp(\frac{v_A - v_j}{\delta_A}))} - g_{A_j}, \\ \dot{\phi}_j &= k_1 v_j - k_2 \phi_j, \end{aligned} \tag{5}$$

where, $W(\phi_j) = \alpha + 3\beta\phi_j^2$. P is the nonlocal coupling range, which is set to $P = 10$ for this study. The magnitude of other parameters are fixed as in Table (1).

Firstly, the collective behavior of a system (5) is investigated by fixing $k_0 = 0.2$ in Fig. 9(i) and (ii) denote the spatiotemporal and snapshots of the dynamical states. At lower coupling strength $D = 0.01$, we observed the desynchronization behavior as shown in Fig. 9a(i), and the neurons are randomly distributed is evident from the snapshot, Fig. 9a(ii). When the coupling strength is increased, it is noticed that transition to traveling wave (TW) (see Figs. 9 c(i)-c(ii)) via traveling chimera (TC) pattern (see Figs. 9 b(i)-b(ii)). In the traveling chimera state, partial oscillators follow the coherent traveling wave pattern while the remaining oscillators exhibit incoherent behaviors in the TW state. Increasing the coupling strength still more, we found that the emergence imperfect traveling chimera (ITC) as depicted in Figs. 9 d(i)-d(ii). The incoherent behavior in the ITC state is suppressed when increasing the coupling strength to $D = 0.35$ (see Figs. 9 e(i)-e(ii)), resulting we observed imperfect traveling wave (ITW). At strong coupling $D = 0.9$, all the neurons result in a coherent synchronization state as illustrated in Figs. 9 f(i)-f(ii).

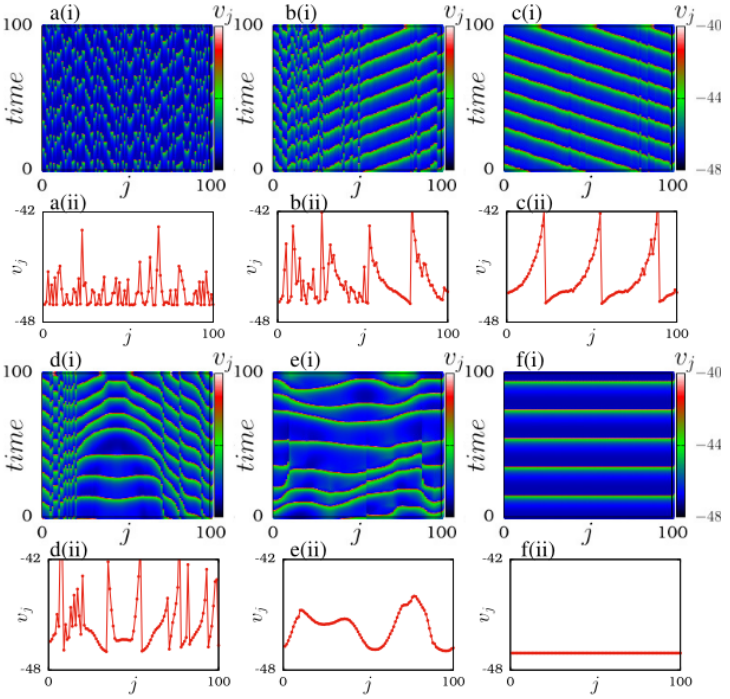

Fig. 9 Space-time (i) and snapshot (ii) images of CadEx neurons, for $k_0 = 0.2$ and $P = 10$, (a) desynchronization ($D = 0.01$), (b) traveling chimera ($D = 0.2$), (c) traveling wave state ($D = 0.22$), (d) imperfect traveling chimera ($D = 0.25$), (e) imperfect traveling wave ($D = 0.35$), and (f) synchronization state ($D = 0.9$). The values for the other parameters are set as given in Table (1). The transition from desynchronization to synchronization via traveling chimera, traveling wave, imperfect traveling chimera and imperfect traveling wave while increasing the nonlocal coupling strength.

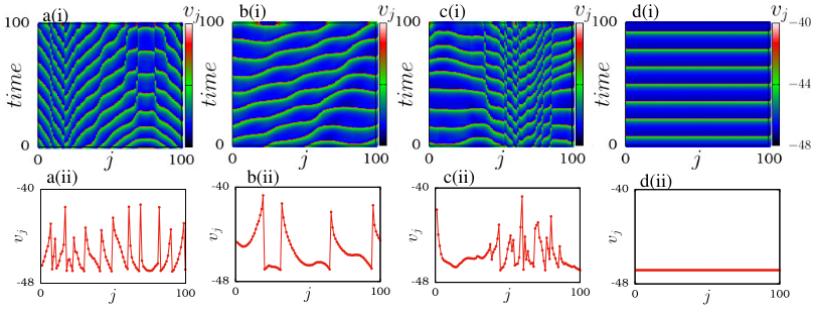

Fig. 10 Space-time (i) and snapshot (ii) images of cadEx by fixing $D = 0.25$ and $P = 10$, (a) imperfect traveling wave for $k_0 = 0.09$, (b) imperfect traveling wave for $k_0 = 0.25$, (c) imperfect chimera for $k_0 = 0.3$, (d)synchronization state for $k_0 = 0.35$. The values for the other parameters are set as given in Table (1). The transition from imperfect traveling wave to synchronization via imperfect traveling chimera while increasing the flux coupling co-efficient.

Analogously, the dynamical transition of system (5) is examined for coupling strength $D = 0.25$ and by fixing different magnitudes of k_0. At lower values of k_0, for $k_0 = 0.09$ and $k_0 = 0.25$, there exist imperfect traveling wave patterns which is evident from Figs. 10 a(i)-a(ii) and Figs. 10 b(i)-b(ii). Further, for $k_0 = 0.3$, the emergence of imperfect chimera behavior is noticed as in Figs. 10 c(i)-c(ii) [49]. Increasing the magnitude of k_0 to 0.35, it is observed that the synchronization state (Figs. 10 d(i)-d(ii)). From the observation, it is clear that the network of CadEx neurons can result in distinct collective dynamics including imperfect chimera and synchronization state depending on the magnitude of flux coupling coefficient and coupling strength.

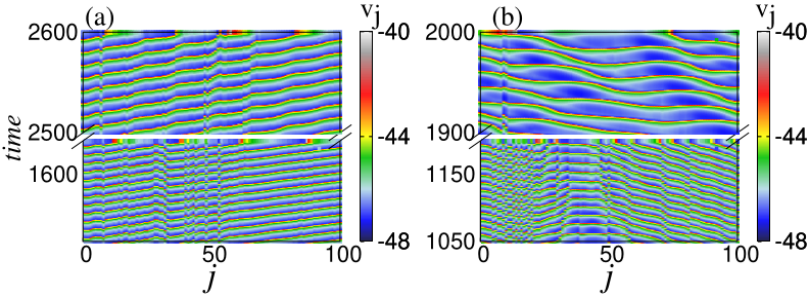

Fig. 11 Space-time images of chimera states by fixing (a) $k_0 = 0.2$ and $D = 0.2$, and (b) $k_0 = 0.25$ and $D = 0.25$. The values for the other parameters are set as given in Table (1). The lower portion of the space-time image represents the dynamics at lower transients, while the upper portion governs the dynamics at longer time periods.

Additionally, we found that as the transient period is increased, the observed traveling chimera and imperfect traveling chimera behaviors disappear. In Figs. 11(a) and 11(b), we showed both chimera states over two distinct time periods to provide additional clarity about the transient behaviors. It is important to notice that chimera behaviors, both coherent and incoherent, were seen at lower transients but vanished as soon as the traveling waves appears. As a result, the chimera states that have been seen are transient chimeras.

5 Conclusion

We have proposed the hybrid adaptive conductance-based exponential integrate and fire neuron model. For a clearer understanding of the dynamical transitions, the bifurcation analysis is carried out with respect to the input current. The bifurcation of period doubling and period halving is observed as the magnitude of the input current decreases, and the existence of period-1, period-2, and period-4 cycles was identified. The bifurcation analysis was also carried out by varying the resetting parameter as well as the adaptation time constant to get a better understanding of the impact of such parameters.

Concerning the adaptation time constant, it is observed that the transition to chaotic behavior is through the period-doubling route. Following that, the network dynamics of hybrid CadEx are examined by varying the flux coupling coefficient or coupling strength, which has yet to be extensively studied in the literature. When increasing the coupling strength, the transition from a desynchronized state to a traveling wave takes place through the traveling chimera. Increasing the coupling strength further gives rise to the transition from an imperfect traveling chimera to synchronization through an imperfect traveling wave. Analogously, the transition from imperfect traveling wave to synchronization was identified through imperfect chimera as varying the flux coupling coefficient. As a result, increasing coupling strength or flux coupling coefficient gives rise to synchronization behaviors via an imperfect chimera state. We demonstrated that introducing memristive effects in CadEx neurons can result in various dynamical transitions depending on the input current, time adaptation constant, and resetting parameter. Furthermore, we demonstrated the presence of rich collective dynamics in a network of coupled CadEx neurons for the first time. The findings of conductance-based neurons might shed insight into the dynamical behavior observed during many cognitive activities in biological systems.

Acknowledgments. We gratefully acknowledge this work is funded by the Center for Nonlinear Systems, Chennai Institute of Technology (CIT), India, vide funding number CIT/CNS/2023/RP-005.

Data availability statement. Data generated during the current study will be made available at reasonable request.

Author Contribution Statement. All the authors contributed equally to the preparation of this manuscript.

References

[1] Trappenberg, T. (2009). Fundamentals of computational neuroscience. OUP Oxford.

[2] Feng, J. (2003). Computational neuroscience: a comprehensive approach. Chapman and Hall/CRC.

[3] Rocsoreanu, C., Georgescu, A., & Giurgiteanu, N. (2012). The FitzHugh-Nagumo model: bifurcation and dynamics (Vol. 10). Springer Science & Business Media.

[4] Storace, M., Linaro, D., & de Lange, E. (2008). The Hindmarsh–Rose neuron model: bifurcation analysis and piecewise-linear approximations. Chaos: An Interdisciplinary Journal of Nonlinear Science, 18(3), 033128.

[5] Nelson, M., & Rinzel, J. (1998). The hodgkin—huxley model. In The book of genesis (pp. 29-49). Springer, New York, NY.

[6] Izhikevich, E. M. (2003). Simple model of spiking neurons. IEEE Transactions on neural networks, 14(6), 1569-1572.

[7] Kanagaraj, S., Durairaj, P., Prince, A. A., & Rajagopal, K. (2022). Local and Network Dynamics of a Non-Integer Order Resistor–Capacitor Shunted Josephson Junction Oscillators. Electronics, 11(18), 2812.

[8] Schöll, E. (2016). Synchronization patterns and chimera states in complex networks: Interplay of topology and dynamics. The European Physical Journal Special Topics, 225(6), 891-919.

[9] Premraj, D., Suresh, K., Banerjee, T., & Thamilmaran, K. (2018). Bifurcation delay in a network of locally coupled slow-fast systems. Physical Review E, 98(2), 022206.

[10] Ramadoss, J., Aghababaei, S., Parastesh, F., Rajagopal, K., Jafari, S., & Hussain, I. (2021). Chimera state in the network of fractional-order fitzhugh–nagumo neurons. Complexity, 2021.

[11] Gerster, M., Berner, R., Sawicki, J., Zakharova, A., Škoch, A., Hlinka, J., Lehnertz, K. & Schöll, E. (2020). FitzHugh–Nagumo oscillators on complex networks mimic epileptic-seizure-related synchronization phenomena. Chaos, 30(12), 123130.

[12] Ibrahim, M. M., Kamran, M. A., Mannan, M. M. N., Jung, I. H., & Kim, S. (2021). Lag synchronization of coupled time-delayed FitzHugh–Nagumo neural networks via feedback control. Scientific reports, 11(1), 1-15.

[13] Rontogiannis, A., & Provata, A. (2021). Chimera states in FitzHugh–Nagumo networks with reflecting connectivity. The European Physical Journal B, 94(5), 1-12.

[14] Premraj, D., Suresh, K., & Thamilmaran, K. (2019). Effect of processing delay on bifurcation delay in a network of slow-fast oscillators. Chaos: An Interdisciplinary Journal of Nonlinear Science, 29(12), 123127.

[15] Paul Asir, M., Sathiyadevi, K., Philominathan, P., & Premraj, D. (2022). A nonlinear memductance induced intermittent and anti-phase synchronization. Chaos: An Interdisciplinary Journal of Nonlinear Science, 32(7), 073125.

[16] Yu, D., Wang, G., Li, T., Ding, Q., & Jia, Y. (2023). Filtering properties of Hodgkin–Huxley neuron on different time-scale signals. Communications in Nonlinear Science and Numerical Simulation, 117, 106894.

[17] Altan, A., & Karasu, S. (2020). Recognition of COVID-19 disease from X-ray images by hybrid model consisting of 2D curvelet transform, chaotic salp swarm algorithm and deep learning technique. Chaos, Solitons & Fractals, 140, 110071.

[18] Yağ, İ., & Altan, A. (2022). Artificial Intelligence-Based Robust Hybrid Algorithm Design and Implementation for Real-Time Detection of Plant Diseases in Agricultural Environments. Biology, 11(12), 1732.

[19] Yu, X., Bao, H., Chen, M., & Bao, B. (2023). Energy balance via memristor synapse in Morris-Lecar two-neuron network with FPGA implementation. Chaos, Solitons & Fractals, 171, 113442.

[20] Ding, S., Wang, N., Bao, H., Chen, B., Wu, H., & Xu, Q. (2023). Memristor synapse-coupled piecewise-linear simplified Hopfield neural network: Dynamics analysis and circuit implementation. Chaos, Solitons & Fractals, 166, 112899.

[21] Li, Z., Tang, W., Zhang, B., Yang, R., & Miao, X. (2023). Emerging memristive neurons for neuromorphic computing and sensing. Science and Technology of Advanced Materials, 24(1), 2188878.

[22] Wang, S., Song, L., Chen, W., Wang, G., Hao, E., Li, C., Hu, Y., Pan, Y., Nathan, A., Hu, G. & Gao, S. (2023). Memristor-Based Intelligent Human-Like Neural Computing. Advanced Electronic Materials, 9(1), 2200877.

[23] Routhu, G., Phalguni Singh, N., & Reddy, E. S. K. (2023). Investigation of Memristor-Based Neural Networks on Pattern Recognition. Engineering Proceedings, 34(1), 9.

[24] Lv, G., Zhang, N., Ma, K., Weng, J., Zhu, P., Chen, F., & He, G. (2021). Functional brain network dynamics based on the Hindmarsh–Rose model. Nonlinear Dynamics, 104(2), 1475-1489.

[25] Parastesh, F., Rajagopal, K., Alsaadi, F. E., Hayat, T., Pham, V. T., & Hussain, I. (2019). Birth and death of spiral waves in a network of Hindmarsh–Rose neurons with exponential magnetic flux and excitable media. Applied Mathematics and Computation, 354, 377-384.

[26] Rajagopal, K., Khalaf, A. J. M., Parastesh, F., Moroz, I., Karthikeyan, A., & Jafari, S. (2019). Dynamical behavior and network analysis of an extended Hindmarsh–Rose neuron model. Nonlinear Dynamics, 98(1),

477-487.

[27] Yang, X., Zhang, G., Li, X., & Wang, D. (2021). Diverse Dynamic Behaviors and Firing Activities of the Modified Fractional-Order Hindmarsh–Rose Neuronal Model Induced by Fractional-Order. Complexity, 2021.

[28] Kafraj, M. S., Parastesh, F., & Jafari, S. (2020). Firing patterns of an improved Izhikevich neuron model under the effect of electromagnetic induction and noise. Chaos, Solitons & Fractals, 137, 109782.

[29] Tolba, M. F., Elsafty, A. H., Armanyos, M., Said, L. A., Madian, A. H., & Radwan, A. G. (2019). Synchronization and FPGA realization of fractional-order Izhikevich neuron model. Microelectronics Journal, 89, 56-69.

[30] Cavallari, S., Panzeri, S., & Mazzoni, A. (2014). Comparison of the dynamics of neural interactions between current-based and conductance-based integrate-and-fire recurrent networks. Frontiers in neural circuits, 8, 12.

[31] Jun, M., Li-Jian, Y., Ying, W., & Cai-Rong, Z. (2010). Spiral wave in small-world networks of Hodgkin–Huxley neurons. Communications in Theoretical Physics, 54(3), 583.

[32] Wang, Q., Shi, X., & Chen, G. (2011). Delay-induced synchronization transition in small-world Hodgkin-Huxley neuronal networks with channel blocking. Discrete & Continuous Dynamical Systems-B, 16(2), 607.

[33] Li, Z., Zhou, H., Wang, M., & Ma, M. (2021). Coexisting firing patterns and phase synchronization in locally active memristor coupled neurons with HR and FN models. Nonlinear Dynamics, 104(2), 1455-1473.

[34] Wang, Z., Guo, L., & Adjouadi, M. (2014). A generalized leaky integrate-and-fire neuron model with fast implementation method. International journal of neural systems, 24(05), 1440004.

[35] Buonocore, A., Caputo, L., Pirozzi, E., & Carfora, M. F. (2016). A leaky integrate-and-fire model with adaptation for the generation of a spike train. Mathematical Biosciences & Engineering, 13(3), 483.

[36] Liu, Y. H., & Wang, X. J. (2001). Spike-frequency adaptation of a generalized leaky integrate-and-fire model neuron. Journal of computational neuroscience, 10(1), 25-45.

[37] Brette, R., & Gerstner, W. (2005). Adaptive exponential integrate-and-fire model as an effective description of neuronal activity. Journal of

neurophysiology, 94(5), 3637-3642.

[38] Ladenbauer, J., Augustin, M., Shiau, L., & Obermayer, K. (2012). Impact of adaptation currents on synchronization of coupled exponential integrate-and-fire neurons. PLoS computational biology, 8(4), e1002478.

[39] Teka, W., Marinov, T. M., & Santamaria, F. (2014). Neuronal spike timing adaptation described with a fractional leaky integrate-and-fire model. PLoS computational biology, 10(3), e1003526.

[40] Santos, M. S., Protachevicz, P. R., Iarosz, K. C., Caldas, I. L., Viana, R. L., Borges, F. S., —- & Grebogi, C. (2019). Spike-burst chimera states in an adaptive exponential integrate-and-fire neuronal network. Chaos: An Interdisciplinary Journal of Nonlinear Science, 29(4), 043106.

[41] Lu, L., Yang, L., Zhan, X., & Jia, Y. (2020). Cluster synchronization and firing rate oscillation induced by time delay in random network of adaptive exponential integrate-and-fire neural system. The European Physical Journal B, 93(11), 1-9.

[42] Yang, S., Wei, X., Deng, B., Liu, C., Li, H., & Wang, J. (2018). Efficient digital implementation of a conductance-based globus pallidus neuron and the dynamics analysis. Physica A: Statistical Mechanics and its Applications, 494, 484-502.

[43] Qi, Y., Watts, A. L., Kim, J. W., & Robinson, P. A. (2013). Firing patterns in a conductance-based neuron model: bifurcation, phase diagram, and chaos. Biological cybernetics, 107(1), 15-24.

[44] Kanagaraj, S., Durairaj, P., Karthikeyan, A., & Rajagopal, K. (2022). Effect of propagation noise on the network dynamics of a flux coupled conductance-based neuron model. The European Physical Journal Plus, 137(11), 1223.

[45] Górski, T., Depannemaecker, D., & Destexhe, A. (2021). Conductance-based adaptive exponential integrate-and-fire model. Neural Computation, 33(1), 41-66.

[46] Lv, M., Wang, C., Ren, G., Ma, J., & Song, X. (2016). Model of electrical activity in a neuron under magnetic flow effect. Nonlinear Dynamics, 85, 1479-1490.

[47] Lv, M., & Ma, J. (2016). Multiple modes of electrical activities in a new neuron model under electromagnetic radiation. Neurocomputing, 205, 375-381.

[48] Wu, F., Wang, C., Xu, Y., & Ma, J. (2016). Model of electrical activity in cardiac tissue under electromagnetic induction. Scientific reports, 6(1), 28.

[49] Sathiyadevi, K., Chandrasekar, V. K., Senthilkumar, D. V., & Lakshmanan, M. (2018). Imperfect amplitude mediated chimera states in a nonlocally coupled network. Frontiers in Applied Mathematics and Statistics, 4, 58.